Advances in Military Technology
Vol. 21, No. 1, 2026, pp. 9-20
ISSN 1802-2308, eISSN 2533-4123
DOI 10.3849/aimt.02015

Evaluation of Flight Parameters for Lidar-Equipped UAS Mapping

H. Picmausová[1,2*], J. Farlík[2], M. Eichhorn[1,3], and C. Kieleck[1]

[1] *Fraunhofer Institute of Optronics, System Technologies and Image Exploitation, Ettlingen, Germany*
[2] *University of Defence, Brno, Czech Republic*
[3] *Institute of Control Systems, Karlsruhe Institute of Technology, Karlsruhe, Germany*

The manuscript was received on 15 July 2025 and was accepted
after revision for publication as an original research paper 6 February 2026.

Abstract:

This article proposes optimization of flight parameters for a Class 1 UAS equipped with multiple sensors in field applications, such as topography and object recognition. A commercial automotive- grade lidar was integrated with a photogrammetry camera on a UAS. A theoretical overview and a numerical model of the system's range and resolution were developed. Multiple area mapping missions were executed over two years with various flight parameters, and atmospheric conditions, using standardized targets to evaluate system performance. Resulting data sets were post-processed, merged, and cross-referenced with satellite imagery. Results were compared to the numerical model and discussed. We propose an optimal use case illustrating how overlaying multi-sensor data enhances object recognition, and we outline directions for future work.

Keywords:

LiDAR, sensor integration, Unmanned Aircraft Systems, 3D area mapping, camera imaging, sensor systems, object classification

1 Introduction

Recently, LiDAR (Light Detection and Ranging) technology has gained significant attention, demonstrating its versatility across a wide range of application fields including autonomous navigation, aerospace and defence, meteorology, and geo-science. LiDAR technology is widely used in combination with other sensors and guidance systems for navigation of autonomous vehicles, area mapping and combat identification [1]. As LiDAR systems become ever more affordable, compact, and robust, and

* *Corresponding author: Laser technology dept., Fraunhofer Institute of Optronics, System Technologies and Image Exploitation, Gutleuthausstraße 1, DE-76275, Ettlingen, Germany. Phone: +420 606 05 28 22, E-mail: Helena.picmausova@iosb.fraunhofer.de. ORCID 0000-0003-3683-7243.*

with a wide range of various solutions available commercially, evaluating their performance for specific applications is crucial [2-4].

Accurate evaluation of the range and performance limits necessitates examining several key parameters. These include the laser source characteristics – such as output power, pulse length and wavelength – as well as the update frequency of the positioning system and atmospheric conditions. One of the major advantages of lidar over many passive sensors is the ability to function in low-light environment. Additionally, when compared to other active sensors like radar, their shorter operating wavelengths result in LiDAR systems achieving higher resolution for a given aperture size due to lower diffraction limit [1, 2, 5].

From defence application point of view, LiDAR mounted on UAV platform gives many opportunities to detect objects of interest. There is a great potential for applications detecting terrain changes like trenches and their depth, debris monitoring and evaluation of their hazard, and more. Great potential also lies in the exploration and detection of objects in forested areas, the monitoring of landscape destruction after the end of fighting, etc. Thanks to the advent of artificial intelligence and the expanding possibilities of quantum computing, it can be expected that more complex algorithms for evaluating LiDAR data will increasingly appear and be promoted [1, 3].

2 LiDAR Deployment Review

Currently, among the most popular laser sources for Range Finders and LiDAR are diode pumped solid-state (DPSS) lasers, which use rare earth materials with relatively long upper-state lifetimes and can produce nanosecond-class pulses through Q-switching. Common laser sources include Nd^{3+}:YAG emitting at 1.064 μm, which despite lower quantum efficiency offers commercial availability and maturity [6, 7].

Diode-pumped fibre laser architectures are increasingly researched and developed across the industry due to their high beam quality, and excellent SWaP (Size, Weight and Power) integration. These systems usually operate in the 1 060–1 100 nm range for Yb-doped fibre lasers, and around 1 550 nm for Er-Yb co-doped fibre lasers. In general, fibre laser systems operating above 1.5 μm can be considered retina-safe, are less susceptible to solar radiation noise, and offer good availability of components due to telecommunication applications [7, 8].

Diode lasers around the 905 nm range are frequently used in flash lidar applications, especially in the automotive sector, owing to low cost, good electrical efficiency and compactness. However, these diode systems cannot provide high peak power, therefore their detection range is limited by the lower pulse energy and lower average power in pulsed operation [9, 10].

Environmental factors play a vital role when evaluating lidar performance. Unlike atmospheric scattering, atmospheric absorption is highly wavelength specific for molecular composition of air. Selecting a suitable wavelength is therefore crucial to minimizing beam power decay over the two-way path between the lidar and the target. Humidity and other local weather conditions highly influence scattering and signal attenuation, especially depending on wavelength [11]. For the wavelengths mentioned above, water absorption peaks at 1 064 nm and is the lowest at 1 550 nm [6].

Ambient illuminance also affects system performance. Detection range notably decreases with high illuminance due to high noise impact on the SPAD detector (Single Photon Avalanche Diode). On bright days, or in highly sunlit environments (e.g.,

around 100 klx), the effective detection range of a lidar can reportedly drop to around 70 % of values achievable during clear night conditions (0 l× in optimal case) [12, 13].

3 Theory and Numerical Results

3.1 LiDAR Equation

The governing principle for power received by a statistic (multi-photon count) detection is the LiDAR equation:

$$P(R) = P_0 \frac{4\sigma(\Omega)}{\pi\omega(R)^2} \frac{A_0\eta_0}{\pi R^2} e^{-2\gamma R} \tag{1}$$

where P_0 is the source power, $\sigma(\Omega)$ is the LiDAR cross-section, ω the laser beam waist at range R, A_0 is the detector optics effective area, η_0 is the overall system efficiency, and γ is the atmospheric extinction coefficient, as illustrated in Fig. 1. This is analogous to the radar equation, with the main distinction being that the operating wavelength is approximately four orders of magnitude shorter than that of a radar. Whereas radars operate up to approximately 40 GHz, lasers in the SWIR (Short-wave infrared) spectrum reach 192 THz.

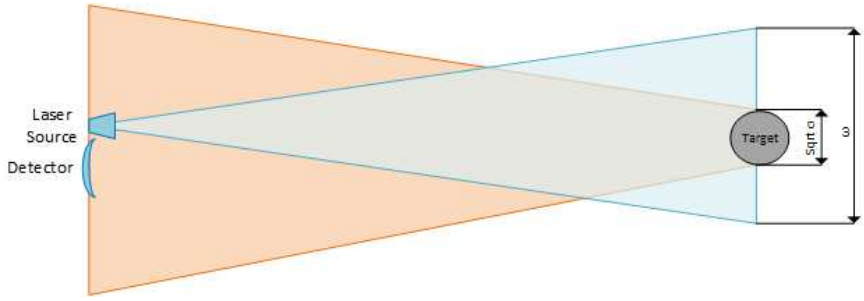

Fig. 1 LiDAR principal schematic

A numerical model was created to assess feasibility of the experiment and to compare analytical values, numerical data, and the experimental results. Using Eq. (1) and assuming a square detector with a 10 cm side, 40 mrad divergence, and a source diode of 30 W peak power, with a top-hat beam profile (parameters corresponding to the experiment). The values in Tab. 1 illustrate the expected analytical number of returning photons detected by the system. For a flash LiDAR system, a minimum number for successful detection is at around 3 photons, highlighted in green. Yellow values show the distance where the signal is still above the noise detection limit, given by dark photon count of a SPAD, but the range can no longer be measured by a single pulse, and red values are under the noise detection limit.

3.2 Numerical Model

A ray-tracing numerical model was developed to compare with the analytically predicted detection limits. Test targets were modelled, comprising of cubes with side lengths of 1, 2, 4, and 8 cm (16 cm largest total dimension), and 10, 20, 40, and 80 cm (160 cm total), as in the example in Fig. 2.

Tab. 1 Number of returning photons expected on the detector, analytical calculation

Range [m]	10	20	50	100	200	500	1000
Target size [m]	No. of detected photons						
0.1	8.10×10^{3}	5.06×10^{2}	1.30×10^{1}	8.10×10^{-1}	5.06×10^{-2}	1.30×10^{-3}	8.10×10^{-5}
0.2	1.62×10^{4}	1.01×10^{3}	2.59×10^{1}	1.62×10^{0}	1.01×10^{-1}	2.59×10^{-3}	1.62×10^{-4}
0.4	3.24×10^{4}	2.03×10^{3}	5.19×10^{1}	3.24×10^{0}	2.03×10^{-1}	5.19×10^{-3}	3.24×10^{-4}
0.8	3.24×10^{4}	4.05×10^{3}	1.04×10^{2}	6.48×10^{0}	4.05×10^{-1}	1.04×10^{-2}	6.48×10^{-4}
1.6	3.24×10^{4}	4.05×10^{3}	2.07×10^{2}	1.30×10^{1}	8.10×10^{-1}	2.07×10^{-2}	1.30×10^{-3}

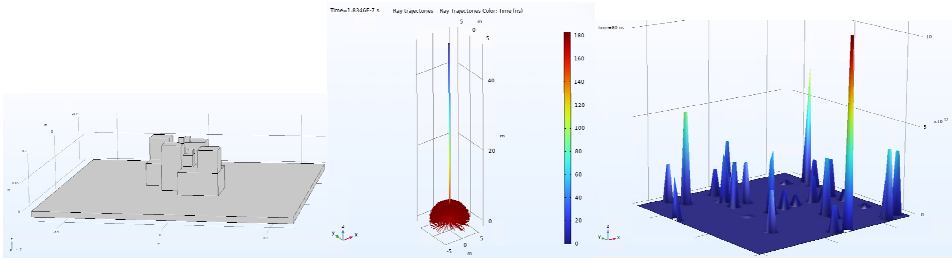

Fig. 2 Numerical model overview: a test target, a ray-tracing model with Lambertian scattering on laser-matter interaction, and photon count on the detector

The model computes ray propagation in homogeneous media and evaluates the corresponding ray intensities. Reflection on material boundaries, as well as refraction, and attenuating media are considered.

Lambert's cosine law is applied at the boundaries causing scattering of rays, as depicted in Fig. 2. Explicitly, the observed ray intensity is directly proportional to the cosine of the angle α between the observer's line of sight and the surface normal. Lambertian, or (in non-ideal case) diffuse scattering is a prerequisite for LiDAR operation.

Overview of returning photons obtained from the numerical model is presented in Tab. 2. Values in green indicate likely and accurate detection based on three-photons detection limit, whereas values in yellow require multiple measurements.

Tab. 2 Number of returning photons expected on the detector, numerical analysis

Range [m]	10	50	100	200
Target size [m]	No. of detected photons			
0.1	9.62×10^{3}	1.54×10^{1}	9.62×10^{-1}	6.01×10^{-2}
0.2	1.93×10^{4}	3.08×10^{1}	1.93×10^{0}	1.20×10^{-1}
0.8	3.85×10^{4}	1.23×10^{2}	7.70×10^{0}	4.81×10^{-1}

Small differences in values in Tabs 1 and 2 are caused by a top-hat beam profile and mitigation of the reflection angle difference in Lambert's cosine law assumed in the LiDAR equation Eq. (1).

4 Experimental Set-up and Objectives

The initial investigation into LiDAR performance was executed in 2023 and is reported on in [14]. Lessons learned during these experiments were applied to a new set of tests conducted in 2024. Additional data processing and evaluation have been performed and are presented in this paper.

The experimental phase aimed at the evaluation of a commercially available automotive grade lidar system under realistic conditions. The system consisted of a flash lidar sensor, an RGB mapping camera, and an Inertial Measurement Unit (IMU), and was mounted on a DJI Matrice 300 RTK Unmanned Aircraft System (UAS).

A dedicated test site was prepared to support repeated mapping missions at different altitudes, also including a variety of terrain features such as varying ground elevation, vegetation, buildings, vehicles, and people. This diverse setting was chosen to provide an opportunity to test sensor performance across a wide range of practical-use cases.

The primary objectives of the initial round of experiments were:

- validation of manufacturer-stated specifications in the product datasheet, particularly the range accuracy and resolution,
- examination of the impact of flight speed and altitude on detection performance of both sensors – the lidar and the camera,
- assessment of the influence of object reflectivity, size, and material on sensor detection, and an evaluation of mutual alignment of the data from the two sensors.

As the setup concerned airborne mapping, precise spatial positioning of the UAS was crucial for the experiment accuracy. And while the UAS navigation systems generally benefit from GNSS technology, the internal IMU inertial navigation is essential for maintaining sensor data consistency. The IMU's update rate directly influences the reliability of the LiDAR data point cloud and sensor data fusion results, as well as accurate measurements of angle/roll, pitch and yaw. The accuracy of data fusion was also an area of interest, as the use for defence applications necessarily requires accurate position information. The measurements were intended from the outset for both civilian and defence applications.

Following the original series of tests carried out in 2023 [14], a second series of flights was conducted in 2024, to refine and optimize flight parameters based on lessons learned during the initial phase of testing. This included adjusting parameters such as flight speed and altitude, scanning FOV and its area overlap, to improve performance and cloud field density. The follow-up tests were conducted to validate and assess the practical benefits of operational adjustments to the sensor system and to refine the optimal use-case scenarios for field deployment.

4.1 Model Targets

In addition to naturally occurring terrain elements and structures, standardized model targets were designed to provide a benchmark reference for the system resolution and detection evaluation, given that test accuracy benefits from adding pre-acquired metric data [15]. The targets were designed specifically for the experiment and manufactured by 3D printing. The goal was to quantify the system's capability to detect objects of varying size, shape and reflectivity. Each design comprised of multiple cube elements with side lengths of 1, 2, 4, and 8 cm positioned to enable resolution testing across horizontal, vertical, and depth axes. The total dimensions of the model were therefore

16 × 16 × 9 cm (W × H × D), and the longest diagonal line was approximately 22.6 cm. Two versions of the design were manufactured – the first featured black and red cubes with lower contrast between the used materials, the second incorporated alternating black and white filament material providing high contrast between the high reflectivity white cubes, and low reflectivity black cubes. The measurements and the manufactured targets are shown in Fig. 3.

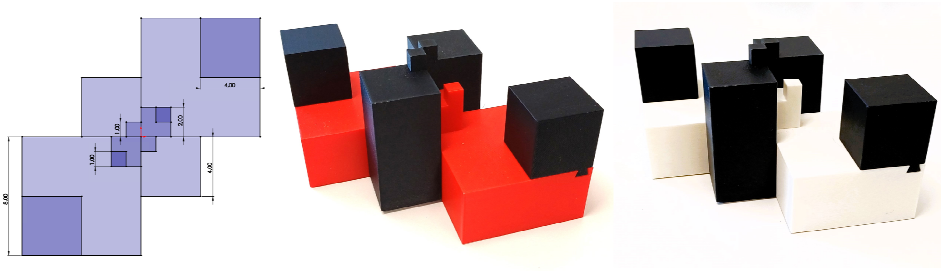

Fig. 3 Original design dimensions and 3D prints of the test targets

4.2 Declared LiDAR Accuracy

The specification of the system, as listed by the manufacturer, were: 905 nm operating wavelength, LiDAR ranging accuracy of 3 cm at a 100 m distance, 30 W system power, IMU update frequency of 200 Hz and a point return rate over 240 000 pts/s, with a detection range reaching over 400 m at 80% reflectivity, and the operating temperature range from −20 °C to 50° C. The official control software offers flight route planning with flight track overlap and angle options, time-of-flight estimation, and postprocessing tools including an overlay of the acquired LiDAR data point cloud and photogrammetry images from the 20 MP, 1” CMOS camera. These values were measured, however, in laboratory environment, with the relative altitude of 50 m, flight speed of 10 m/s, gimbal pitch at −90°, and a 5-minute warm-up. Based on these values, 50 m and 100 m altitude flights were executed during the experiment, with flight speeds between 10 m/s and 15 m/s, and test targets as described above.

4.3 Flight Conditions

Mapping missions were conducted at two flight altitudes: 50 m and 100 m above the ground level. These altitudes were selected to assess the influence of flight height on resolution and object detection accuracy. The mission planning software allows to create a flight route that covers the target area by dividing it into stripes corresponding to a back and forth path with off-set U-turns at the area edge, as shown in the example in Fig. 4. The software allows for overlap setting of scanned stripes as well, these values were set at 20 % for the 50 m altitude flights and 50 % for the 100 m flights, to ensure sufficient area coverage and captured data redundancy. Another key parameter is the flight speed of the UAS; for flights conducted in 2023, the speed was set to 15 m/s, for the follow-up sequence in 2024 it was reduced to 10 m/s. The flights were performed under stable, clear weather conditions. The temperatures were approximately 18 °C in 2023 and 21° in 2024 with relative humidity below 30 %, and wind conditions remaining calm throughout the data acquisition period. Scans were conducted during full daylight to test system performance under high ambient

illuminance, which is known to reduce detection range and increase background noise. Reference images of the test area were captured by the onboard RGB camera, as shown on the example image in Fig. 5. The environmental setting is illustrated in the image, including tents, storage, cables, and several people present on the screen.

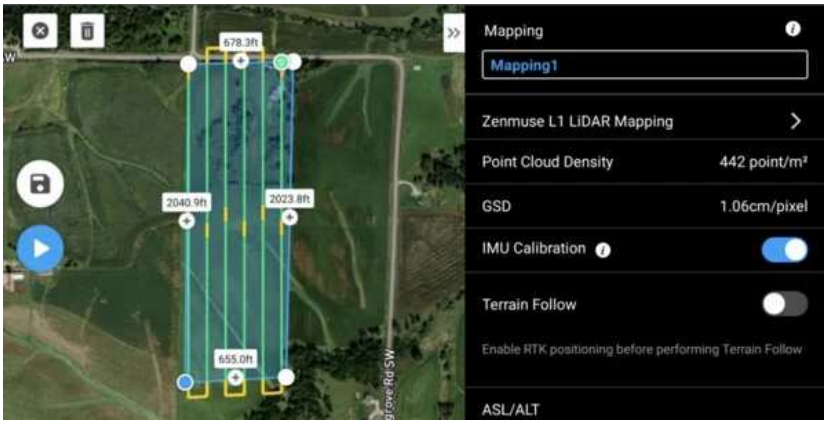

Fig. 4 An example of a flight path created for an area mapping mission, referenced from [16]

Fig. 5 A photo taken by camera from a 100 m *altitude flight*

5 Results and Data Processing

5.1 Flight Data Overview

Fig. 6 shows the overlay of the lidar point cloud with photogrammetric data captured at 50 m flight altitude, then the same dataset colorized according to measured reflectivity levels, and finally a colorization according to ground point classification. Notably, the white tent present in the scene was only partially detected by the LiDAR

system – its side facing the detector at a shallow scanning angle remained undetected. This phenomenon, also observed in similar studies [15], can be mitigated by conducting multiple scans at different angles or applying energy-balancing algorithms in post-processing. A slight improvement to this phenomenon is visible later in Figs 7 and 8, where the point clouds from different flights at different altitudes are merged in the post-process. The merging of data was carried out in the second year of measurements, as original datasets from both altitudes encountered the issue of scanning incidence angle data loss.

Another noteworthy aspect of the system is visible in the middle images in Figs 6 and 8, where the bright red areas do not truly indicate high reflectivity surfaces. Instead, these are likely scan overlaps where the software interpreted a denser point cloud as increased reflectivity. The misinterpretation highlights the importance of understanding how post-processing software handles the sensor data. The third instance in Fig. 6 shows a different colorization mode based on ground point recognition and can offer better clarity than reflectivity or height mapping, or photogrammetry colorization.

The small, standardized test target was effectively invisible in the point cloud at 50 m altitude, with 15 m/s flight speed. During flights at 15 m/s, only a low number of points was detected by the SPAD sensor at both altitudes, which was insufficient for reliable identification of the model geometry from Fig. 3.

At the 100 m altitude, 15 m/s flight speed, resolution and object classification were further reduced. Even larger features, such as individuals standing in the direct line of sight, became indistinct in the LiDAR data.

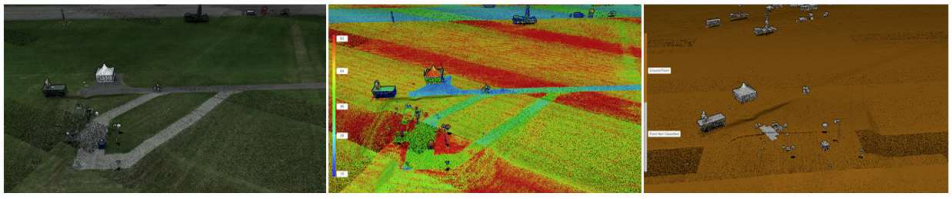

Fig. 6 Results from the 50 m *altitude flights: lidar point cloud overlayed with photogrammetry, a colorization according to reflectivity levels, and a colorization according to ground point classification.*

Fig. 7 Results of lidar point cloud overlayed with photogrammetry: The 100 m *altitude flight,* 50 m *altitude flight, and a combination of both datasets.*

Additional mapping was performed in a nearby area at a road crossing, with a treeline, and several parked cars. Fig. 8 depicts the data processed in a similar way to the previous scene: A photogrammetry and LiDAR point cloud overlay of combined results from flights at both altitudes, a reflectivity-based colorization, and a ground point recognition post processing. While the issue of point-cloud overlap being pre-

sented as higher reflectivity remained, the algorithm successfully distinguished between vegetation and vehicles and classified the asphalt road as ground. It is also possible to filter away objects and vegetation and thus reveal the ground terrain. Additionally, variations in reflectivity among the vehicles were recorded – this was likely due to their paint colours. This example highlights the importance of using multiple analysis modes to compensate for detection limitations of each approach.

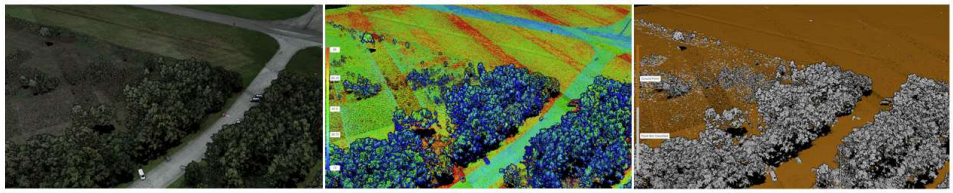

Fig. 8 Combined 50 m *and* 100 m *altitude flight results in a different scene, colorization according to reflectivity levels in the same scene, and ground point recognition.*

Another post processing tool utilized in unmanned surveillance is the generation of a DEM (Digital Elevation Model) from the lidar point cloud. An example of this model is in Fig. 9, combined for comparison with satellite imagery. The image shows the wider area of the location in previous figures.

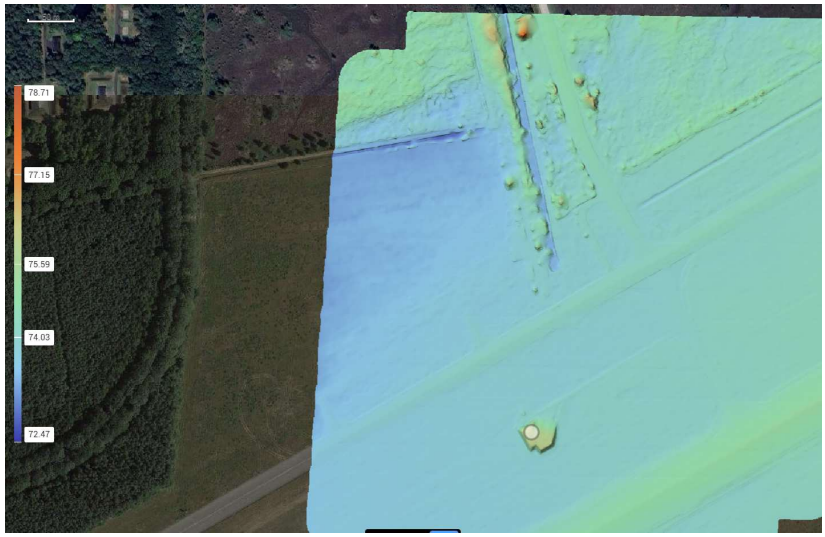

Fig. 9 Comparison of DEM and satellite data.

6 Discussion and Conclusions

Commercial Flash-LiDAR sensors, especially those developed for the automotive sector, are becoming increasingly compact and accessible. When integrated into a system of complimentary sensors, such as RGB cameras, and mounted on unmanned platforms, they offer promising capabilities for mapping, object detection and environmental monitoring. However, their field performance is highly dependent on environmental conditions and operating parameters.

This study demonstrated that the tested lidar system is well suited for terrain mapping and detection of large objects such as buildings, vehicles, and trees: corresponding to the analytic and numerical models, a 50 m altitude flight using a 20–30 W diode as a source can detect objects of 10–20 cm in size, a 100 m altitude up to 40-80 cm, and this resolution diminishes significantly with flight altitude, speed, and target surface reflectivity. Post-processing offers a wide range of applications, including elevation measurement, overgrowth filtering and reflectivity measurement. The interface provides real-time mapping mission planning, and intuitive controls, requiring no additional training for the UAS operator.

The manufacturer-stated specifications correspond to near-optimal conditions, therefore practical limitations must be established and kept in mind, as was verified during the field testing, especially when attempting to detect small targets.

During the study, it became apparent that flight speed, as well as flight altitude play a key role in the lidar detection resolution. The test target, with total of 22.6 cm in diameter, was visible in the point cloud for flights at 50 m altitude, and not at 100 m altitude. This result aligns closely with the model's prediction. For lower flight speed of 10 m/s, a denser point cloud could be obtained to distinguish more detailed features like the 8 cm cube parts, however the smaller details were under the detection limit for both types of the model target. The reflectivity of the material used did not play a pivotal role compared to the flight parameters. Only when dealing with larger targets like cars and tents, the influence of material properties becomes apparent; coated metal objects were observed to provide higher reflectivity for the given wavelength than polymer plastic. However, a detailed analysis of the influence of material surface properties is still under investigation. For a successful mapping of the entire test model, an even lower flight altitude and speed would be necessary, generating a denser point cloud, and thus requiring more memory and computational power for post-processing. Alternatively, the source diode could be replaced by a compact fiber laser source, providing higher peak power (on the order of kW) and thereby significantly extending the range and improving resolution limits.

From the application standpoint, the tested sensor system is well suited for mapping recent terrain changes such as trenches, roadblocks and debris larger than 8-10 cm when operating from a 50 m altitude at a maximum of 10 m/s. In contrast, the setup has limited capability in identifying small objects like Class I UAS in the Micro category, handguns, mines, small munitions etc.

Further studies in the coming years are planned, with flight altitudes of 25 m or even 10 m, flight speeds not exceeding 10 m/s, and potentially a larger standardized test target. This will enable proper verification of the system's LiDAR capabilities.

Funding

The work presented in this article was supported by the Czech Republic Ministry of Defence – the University of Defence development program "DZRO – Conduct of Airspace Operations".

Acknowledgment

The authors would like to thank the Exercise Control Team of the NATO Counter – Unmanned Aircraft Systems Technical Interoperability Exercise 2023 and 2024 (NATO C-UAS TIE 23, NATO C-UAS TIE 24), for their invaluable support in the

realization of the series of experiments: for providing technical facilities, equipment and a dedicated test area, as well as for their extensive expertise, helpful advice and positive attitude.

References

[1] MAINI, A.K. *Handbook of Defence Electronics and Optronics: Fundamentals, Technologies and Systems*. Chichester: Wiley, 2018. ISBN 1-119-18470-3.

[2] McMANAMON, P. *Field Guide to Lidar*. Washington: SPIE, 2015. ISBN 1-62841-655-6.

[3] DAVID, L.C.G., A.H. BALLADO, S.M. SARTE and R.A. PULA. Mapping Inland Aquaculture from Orthophoto and LiDAR Data Using Object-Based Image Analysis. In: *2016 IEEE Region 10 Humanitarian Technology Conference (R10-HTC)*. Agra: IEEE, 2016. DOI 10.1109/R10-HTC.2016.7906855.

[4] WELTON, E.J., et al. The NASA Micro Pulse Lidar Network (MPLNET): Early Results from Development of Diurnal Climatologies. In: *2021 IEEE International Geoscience and Remote Sensing Symposium (IGARSS)*. Brussels: IEEE, 2021. DOI 10.1109/IGARSS47720.2021.9553788.

[5] LIU, J.-K., K.-T. CHANG, C. LIN and L.-C. CHANG. Accuracy Evaluation of ALOS DEM with Airborne LiDAR Data in Southern Taiwan. In: *2015 IEEE International Geoscience and Remote Sensing Symposium (IGARSS)*. Milan: IEEE, 2015, pp. 3025-3028. DOI 10.1109/IGARSS.2015.7326453.

[6] EICHHORN, M. *Laser Physics: From Principles to Practical Work in the Lab*. Cham: Springer, 2014. ISBN 3-319-05127-X.

[7] LARAT, C., M. SCHWARTZ, E. LALLIER and E. DURAND. Eye-Safe Q-Switched Er:YAG MOPA Laser System. In: *Advanced Solid-State Lasers Congress*. Paris: Optica Publishing Group, 2013. DOI 10.1364/ASSL.2013.JTh2A.47.

[8] HOLMEN, L., G. RUSTAD and M. HAAKESTAD. Eye-Safe Fiber Laser for Long-Range 3D Imaging Applications. *Applied Optics,* 2018, **57**(23), pp. 6760-6767. DOI 10.1364/AO.57.006760.

[9] KNIGGE, A., et al. Wavelength Stabilized 905 nm Diode Lasers in the 100 W Class for Automotive LiDAR. In: *2019 Conference on Lasers and Electro-Optics Europe and European Quantum Electronics Conference*. Munich: IEEE, 2019. DOI 10.1109/CLEOE-EQEC.2019.8872824.

[10] LAUGUSTIN, A., C. CANAL and O. RABOT. State-of-the-Art Laser Diode Illuminators for Automotive LIDAR. In: *2019 Conference on Lasers and Electro-Optics Europe & European Quantum Electronics Conference (CLEO/Europe-EQEC).* Munich: IEEE, 2019. DOI 10.1109/CLEOE-EQEC.2019.8872262.

[11] REFAAT, T.F. et al. Backscatter 2-μm Lidar Validation for Atmospheric CO_2 Differential Absorption Lidar Applications. *IEEE Transactions on Geoscience and Remote Sensing*, 2011, **49**(1), pp. 572-580, DOI 10.1109/TGRS.2010.2055874.

[12] KYBA, C., A. MOHAR and T. POSCH. How Bright is Moonlight? *A&G Astronomy and Geophysics*, 2017, **58**(1), pp. 1.31-1.32. DOI 10.1093/astrogeo/atx025.

[13] *LIVOX AVIA. User Manual* [online]. [viewed 2025-05-09]. Available from: https://terra-1-g.djicdn.com/65c028cd298f4669a7f0e40e50ba1131/Download/Avia/Livox%20Avia%20User%20Manual%20202204.pdf

[14] PICMAUSOVÁ, H., J. FARLÍK, M. EICHHORN and C. KIELECK. Lidar Systems Testing Considerations for Field Use. In: *30th Annual STUDENT Electrical Engineering, Information Science, and Communication Technologies Conference, EEICT 2024. Proceedings II of the Conference Student EEICT*. Brno: IOSB, 2024. DOI 10.13164/eeict.2024.192.

[15] BODENSTEINER, C., W. HÜBNER, K. JÜNGLING, P. SOLBRIG and M. ARENS. Monocular Camera Trajectory Optimization Using LiDAR Data. In: *2011 IEEE International Conference on Computer Vision Workshops (ICCV Workshops).* Barcelona: IEEE, 2011, pp. 2018-2025. DOI 10.1109/ICCVW.2011.6130496.

[16] *Mastering LiDAR with DJI Enterprise: An Introductory Booklet* [online]. [viewed 2025-05-02]. Available from: https://enterprise-insights.dji.com/blog/lidar-basic-guide